Thin-Walled Structures 182 (2023) 110261

Contents lists available at ScienceDirect

Thin-Walled Structures

journal homepage: www.elsevier.com/locate/tws

Full length article

Investigation of penetration behavior of combined geometry shells at quasi-static and intermediate strain rates: An experimental and numerical study

Ali Kivanc Turan, Alper Tasdemirci *, Ali Kara, Selim Sahin, Mustafa Guden

Dynamic Testing and Modeling Laboratory, Turkey
Department of Mechanical Engineering, Izmir Institute of Technology, Gulbahce, Urla, Izmir, Turkey

ARTICLE INFO

Keywords:
Penetration behavior
LSDYNA
Micro-inertia
Strain rate sensitivity

ABSTRACT

In this study, the penetration/perforation behavior of a core material with previously determined static and dynamic crushing characteristics was investigated both experimentally and numerically. Penetration/perforation problems occur due to shrapnel effect when sandwich structures containing energy-absorbing core materials by crushing are exposed to blast loads. The penetration behavior of combined geometry shells consisting of a hemispherical cap and a cylindrical segment was investigated experimentally using blunt, conical and hemispherical penetrator tips. The quasi-static penetration tests were performed in a universal test machine, and the intermediate strain rate penetration tests were performed in a drop weight test device. The numerical models of penetration tests were implemented in LS-DYNA at the test strain rates as well as at the higher strain rates. Results showed that different penetrator geometries induced damage forms of symmetrical tearing, petaling, plugging and inversely formed hemispherical domed cone. The increase in the thickness of core geometry resulted in a decent increase in force–displacement curves, as average of force levels increased around 140%, 200% and 220% for blunt, conical and hemispherical tip penetrators, respectively. Numerical results indicated very good correlation with experimental work and enabled to investigate effect of strain rate and micro-inertia over numerical models at elevated penetrator velocities. Penetration behavior was found to be affected from micro-inertia effects up to a threshold displacement of 4 mm for thicker and 5 mm for thinner core units and strain rate effects were found to be dominant beyond that point.

1. Introduction

High-strength thick-monolithic metal plates are conventionally used to provide protection against bullets [1–3]. A higher protection level is merely achieved in metal armors by an increase in the thickness of plate, usually resulting in an excessive increase in the total weight. Metal armors have gradually being replaced by multi-layered material systems. A typical example is the integrated composite armor, which is mainly composed of functionally different two material layers. A hard ceramic front layer effectively deforms the penetrator, reducing its velocity and a composite backing layer absorbs the residual kinetic energy of penetrator, avoiding its full penetration [4–7]. Apparently, the so-called sandwich armor structures are a kind of new versions of multi-layered armor structures, enabling advance design of armors with enhanced strength and weight properties. Various face plates and cores in different forms and geometries are investigated in the sandwich armor structures, and their ballistic performance are determined by their components' mechanical properties, both individually and as a combination. Each component of a sandwich armor structure has its own characteristics and core units play an important role in the absorption and dissipation of impact energy. The ballistic performances of sandwich structures with different faces and core units have been widely studied, the examples of which can be found in the following Refs. [8–19]. Jover et al. investigated the ballistic performance of carbon fiber face and backing plates with balsa wood core units under steel sphere impact with a single stage gas gun [20]. Single and multi-stage gas gun tests indicated a ballistic limit of 96 m s^{-1} for the proposed geometry. Impact tests conducted during the study indicated that balsa wood core is stiffer whereas PVC foam core has the ability to reduce the delamination area on the non-impacted side. Inverse perforation of sandwich panels with aluminum foam-like core structures were also investigated by Zhao et al. [21]. Experimental study was done using a modified Split Hopkinson Pressure Bar to conduct inverse perforation tests which was able to reach the impact velocities around 46 m·s^{-1}. Penetration behavior of metallic and polymeric foams were used as core units and their ballistic performance was studied by Tasdemirci et al. [22]. Penetration behavior of sandwich armor structures with Teflon, rubber,

* Correspondence to: Izmir Institute of Technology, Gulbahce Koyu, Urla, Izmir 35430, Turkey.
E-mail address: alpertasdemirci@iyte.edu.tr (A. Tasdemirci).

https://doi.org/10.1016/j.tws.2022.110261
Received 25 February 2022; Received in revised form 15 August 2022; Accepted 10 October 2022
Available online xxxx

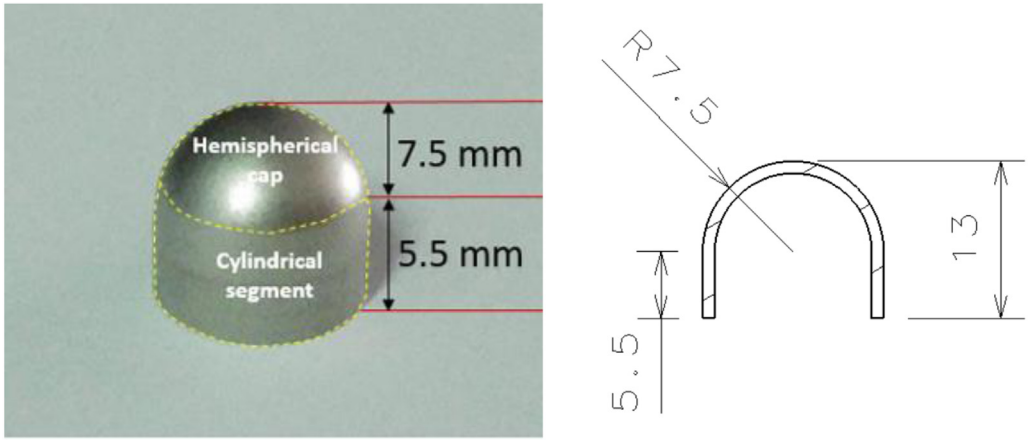

Fig. 1. A picture of a shell unit with its segments and dimensions.

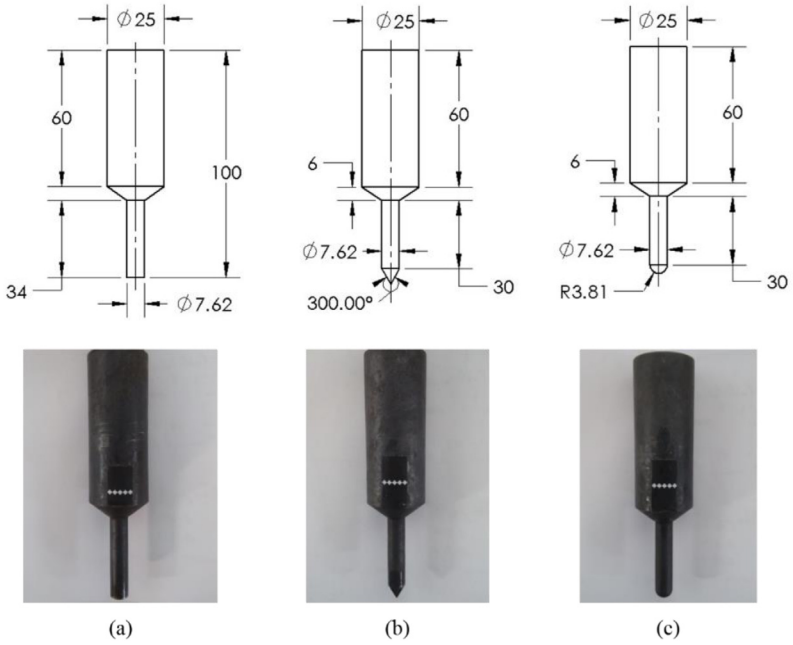

Fig. 2. Geometric dimensions and images of the penetrators used in quasi-static tests; (a) blunt, (b) conical, and (c) hemispherical tip.

aluminum foam was compared against the structure without a core unit against impact velocities ranging between 790–810 m s^{-1}. Study concluded that Teflon and aluminum foam cores significantly reduced the stress on backing plate. In an event of explosion from a landmine or improvised explosive device (IED) with close stand-off distance, both blast wave and blast propelled shrapnel were produced. It is expected from an armor structure to withstand both of these threats. In this study, the penetration/perforation behavior of a core material with previously determined [23–25] static and dynamic crushing characteristics was investigated both experimentally and numerically. In addition to determining the energy absorption characteristics of such structures, which protect against blast by absorbing energy, it is also very important to examine the penetration and perforation behavior of the structures against pointed or blunt shrapnel like geometries that occur during explosion. For this reason, in this study, the effect of different geometry tips on the penetration performance of the cores was investigated instead of ballistic threats. The penetration behavior of combined geometry shells consisting of a hemispherical cap and a cylindrical segment was investigated experimentally using blunt, conical and hemispherical penetrator tips. The quasi-static penetration tests were performed in a universal test machine, and the intermediate strain rate penetration tests were performed in a drop weight test device. The numerical models of penetration tests were implemented in LS-DYNA at the test strain rates. Once the quasi-static and drop weight numerical models presented the experimental behavior accurately, the study was continued with higher impact velocities. In this way, it was possible to distinguish the contribution of two main effects, which were thought to be effective on the behavior at high deformation rates: the material's strain rate sensitivity and micro inertia. The strain rate parameter in the material model was activated and deactivated and the solutions were repeated. Then, the results were compared for the two extremities. As a result, in this study, the effect of some important variables on the penetration/perforation behavior that could not be distinguished experimentally was investigated by using a verified numerical model at higher impact velocities.

2. Experimental study

2.1. Materials

The investigated combined geometry shell structure (shell unit) consisted of a hemispherical cap and a cylindrical segment, Fig. 1. The

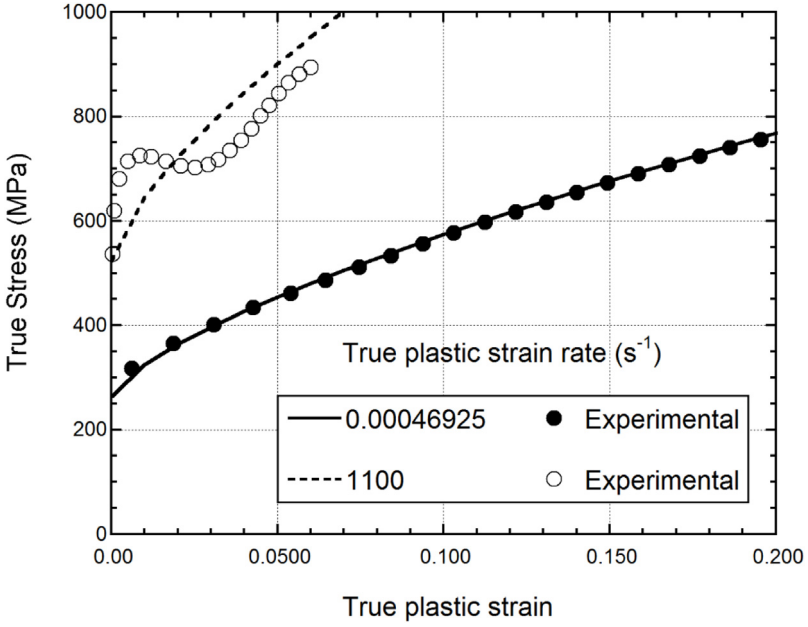

Fig. 3. Experimental tensile stress–strain curves of AISI 304L steel at quasi-static and high strain rates and corresponding Johnson–Cook model fits [24].

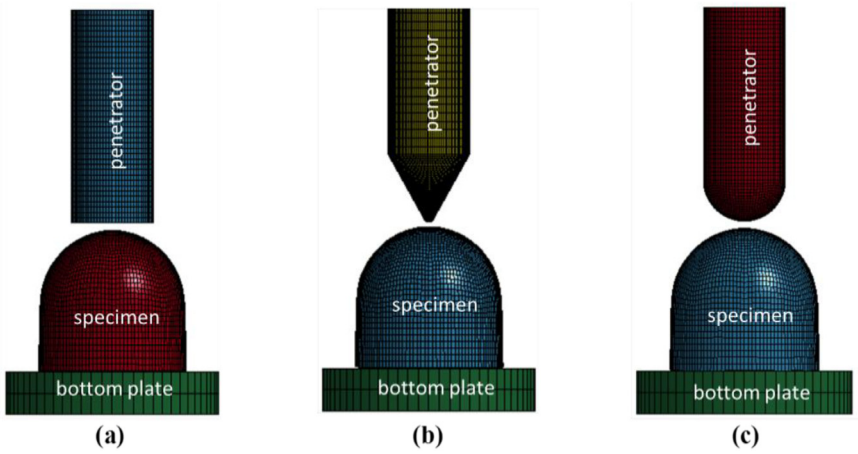

Fig. 4. Numerical models of (a) blunt, (b) conical, and (c) hemisphere tip penetration tests.

shell units were manufactured by a deep drawing process using 304L stainless steel blanks. The wavy edge of shell units resulted from the applied deep drawing process were cut using a CNC lathe. The shell units were formed with a hemispherical-cap radius of 7.5 mm and a cylindrical-segment length of 5.5 mm, either in 0.5 mm or in 1 mm thicknesses (Fig. 1). The units with 0.5 and 1 mm thicknesses were coded S1 and S2, respectively.

2.2. Quasi-static and intermediate velocity penetration tests

Quasi-static penetration tests were performed in a Shimadzu AG-X conventional test device at three different cross-head speeds, 0.013, 0.13 and 1.3 mm s^{-1}, using custom design penetrators. A video extensometer was used to record the displacement of penetrators during penetration tests. Each group of penetration tests was repeated at least three times, and the results were then averaged. The penetrators were machined from an AISI 4140 steel and hardened to 52 HRC by applying a post heat-treatment process. The penetrators with a common diameter of 7.62 mm that was the same as the NATO armor piercing rounds [26], were manufactured in three different tip geometries, namely blunt, hemisphere and conical. The penetrators and their dimensions are shown in Fig. 2.

Intermediate velocity penetration tests were carried out in a Fractovis Plus drop weight test machine using the penetrators with the same tips (attached to the end of a strain-gaged striker of the drop weight test machine) as with the quasi-static penetration tests, except the hemispherical tip penetrator. In tests using hemispherical tip penetrator, it was determined that there was a slip due to the geometrical confirmation between the hemispherical tip and the hemispherical part of the sample. For this reason, hemispherical tip was not used in intermediate strain rate tests, since it was determined that a similar slip would occur in the drop weight tests. In case of slippage, there is a high probability that the tip will slide directly without penetrating the sample surface and damage the lower support plate. Tests were conducted at an impact velocity of 3.5 m s^{-1} using a strain gaged 90 kN striker. The 5.75 kg mass selected in the drop weight tests was determined by the energy values calculated by considering the quasi-static force displacement curves. Again, each group of intermediate velocity penetration tests was repeated at least three times and the results were then averaged.

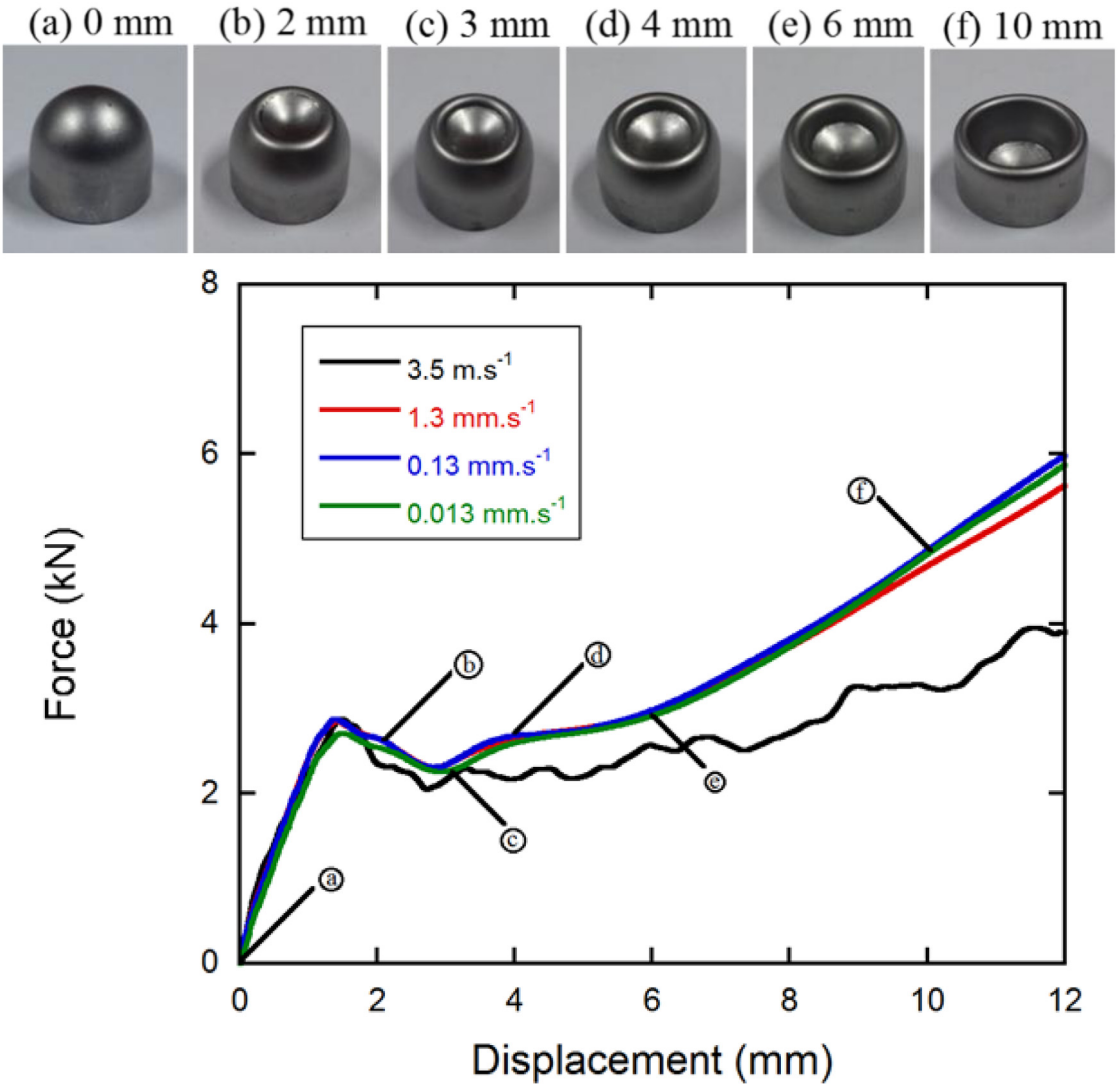

Fig. 5. Force–displacement curves of S1 specimen and deformation progress against blunt tip penetrator.

3. Numerical study

All numerical investigations were implemented in LS-DYNA. As the details of the models are given in another study [24] and the dynain methodology was used to consider the residual stress and residual strain effects that occur in the structure during deep drawing. In this methodology, first the deep drawing is modeled numerically and then the deep drawn numerical sample containing residual stress and strain is used as input to the next numerical model. Thus, in the next step, penetration into the sample containing residual stresses and strains in the penetration numerical model was performed. The details of the numerical deep drawing process were given previously in [23–25]. The combined geometry shells were modeled using the Johnson–Cook (JC) material flow stress model given as [27]

$$\sigma_{eq} = \left[A + B{\varepsilon_{eq}}^{n}\right]\left[1 + c\ln(\frac{\dot{\varepsilon}_{eq}}{\dot{\varepsilon}_0})\right]\left[1 - \left(\frac{T - T_r}{T_m - T_r}\right)^{m}\right] \quad (1)$$

where, σ_{eq} and ε_{eq} are sequentially the equivalent stress and plastic strain, A, B, n, c and m are the material constants to be determined, $\dot{\varepsilon}_{eq}$ is the equivalent plastic strain rate, $\dot{\varepsilon}_0$ is the user defined reference plastic strain rate and T, T_r and T_m are the temperature, room temperature and melting temperature, respectively. The damage was modeled using the JC damage model, given as [27]

$$\varepsilon_f = \left[D_1 + D_2 e^{D_3\sigma^*}\right]\left[1 + D_4\ln\left(\frac{\dot{\varepsilon}_{eq}}{\dot{\varepsilon}_0}\right)\right]\left[1 + D_5\left(\frac{T - T_r}{T_m - T_r}\right)\right] \quad (2)$$

where ε_f is the equivalent plastic fracture strain, D_1, D_2, D_3, D_4 and D_5 are the damage parameters to be determined, and σ^* is the stress triaxiality defined as $\sigma^* = \frac{\sigma_m}{\sigma_{eq}}$, where σ_m is the mean stress. As the stress triaxiality does not change significantly during compression and the tests were performed at room temperature without any heating of unit shell during penetration process, the stress triaxiality and thermal effects are neglected. Thus, the fracture strain is simplified into the following relation,

$$\varepsilon_f = D_1\left[1 + D_4\ln\left(\frac{\dot{\varepsilon}_{eq}}{\dot{\varepsilon}_0}\right)\right] \quad (3)$$

The JC flow stress and damage parameters of the investigated unit shells were determined and reported in a previous study [24], and are also tabulated in Table 1. For the numerical model of the penetration/perforation behavior, the elastic and plastic constitutive behavior of as-received AISI 304L stainless steel sheets were determined at both static and high strain rates. The static tension tests were carried out in accord with ASTM E8M-04 at the strain rates of 10^{-3}, 10^{-2} and 10^{-1} s^{-1} using a Shimadzu universal test machine and high strain rate tests were carried out in a tensile Split Hopkinson Pressure Bar (SHPB) at the average strain rates of 1100 and 1400 s^{-1}. The details of the used 316L stainless steel bar tensile SHPB and the methodology of obtaining material model constants are given elsewhere [24]. The displacement history of static test specimens were recorded using a

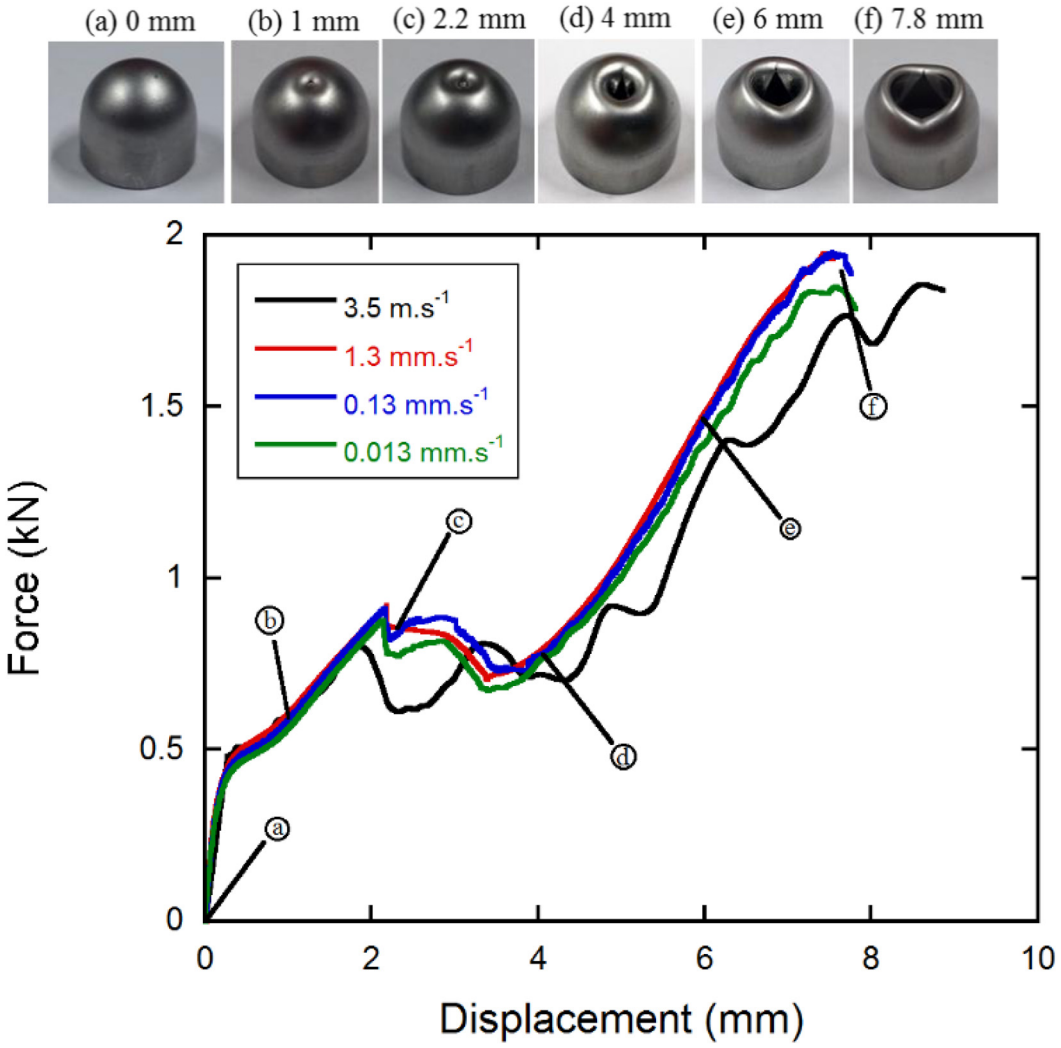

Fig. 6. Force–displacement curves of S1 specimen and damage progress against conical tip penetrator.

Table 1
The JC flow stress and damage parameters used in the numerical model [24].

ρ (kg/m^3)	G (GPa)	E (GPa)	υ	A (MPa)	B (MPa)	n	C	D_1	D_4	ε_0
7830	80	193	0.305	264	1567.33	0.703	0.067	0.53467	−0.01913	0.0049

video extensometer, while a high speed camera was used to monitor the deformation during the SHPB tests. Typical static and high strain rate true stress–true plastic strain curves of AISI 304L stainless steel are given in Fig. 3 [24]. The material shows a strong strain rate dependent flow stress as seen in Fig. 3 [24]. The yield stress increases from about 230 MPa at quasi-static strain rate to about 475 MPa at high strain rate. The fracture strain is also found strain rate dependent; the fracture strain decreases from about 0.6 at quasi-static strain rate to about 0.3 at high strain rate. The damage equation of the material model used represents the effect of strain rate on the failure strain with parameter D_4. The D_4 value was calculated to be negative in the current study since the failure strain value decreased as the strain rate increased. As elaborated in detail in the modeling section, a constitutive model incorporating the effect of strain rate on both strength and failure strain was used in the simulations.

The finite element models of the penetration tests consisted of 3 parts as depicted in Fig. 4: (a) penetrator, (b) unit shell generated from deep drawing analysis and (c) bottom plate. Since it was observed that no significant amount of deformation occurred in the penetrator and the lower support plate during the tests, these two parts were modeled as rigid in the numerical models. The penetrator was allowed to move only in the height direction, while the bottom plate was fully constrained. The movement of the penetrator in the quasi-static tests was defined by the BOUNDARY_PRESCRIBED_MOTION_RIGID card, which included a constant crosshead velocity only in the penetration direction as with the tests. INITIAL_VELOCITY_RIGID_BODY card was used to define the motion of penetrator in the drop weight test models. In the numerical model of the drop weight tests, the penetrator tip and the striker are modeled together to stay within the acceptable solution times. For this reason, part-based mass lumping was used to reach the total mass of the penetrator attached to the striker. In this method, LSDYNA automatically calculates the mass that needs to be added and includes it in the numerical model. In both numerical models, quasi-static and intermediate velocity penetration, penetrators and unit shells were modeled using Belytschko–Tsay shell elements with five integration points, while the bottom plate was modeled using 8-node constant stress solid elements. Automatic surface to surface contact definition was used between the bottom plate and the unit shell. For

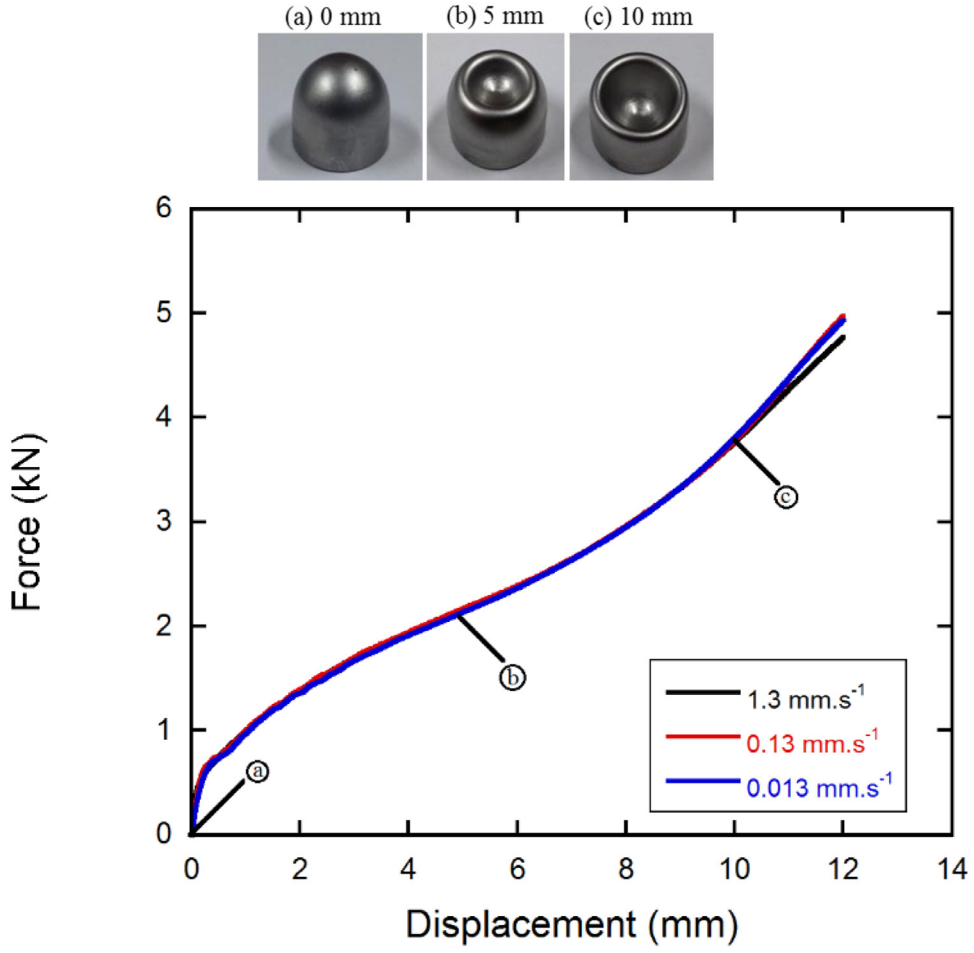

Fig. 7. Force–displacement curves of S1 specimen and damage progress against hemispherical tip penetrator.

the definition of contact between penetrator and sample, eroding nodes to surface and eroding single surface contact definitions were used for conical tip and blunt tip penetrators, respectively, depending on the type of penetrator.

The static and dynamic friction coefficients at all contacts were taken 0.3 and 0.2, respectively. The aforementioned values were also used in previous studies for the static and dynamic compression numerical models of the same core unit [23–25], and a good consistency between the experimental and numerical results was noted. As the penetration problems involve a high amount of plastic deformation and tearing, numerical model requires the optimization of contact and mesh sizes, mesh sensitivity analyses were conducted for each penetrator type. An optimized element size of 0.5 mm was determined from these analyses by keeping the solution times within acceptable limits and accuracy levels.

4. Results and discussion

4.1. Experimental results and damage progress

In the blunt tip penetrator, the deformation of S1 specimen tested at 0.013 mm·s^{-1} is initiated by inward dimpling of spherical segment up to a threshold displacement of 4 mm (d in Fig. 5). Beyond that point, the deformation of the cylindrical segment by the progressive folding in the longitudinal direction starts (e and f in Fig. 5). This results in a simultaneous increase of force with increasing displacement. The longitudinal folding mechanism results in a plug formation and the failure occurs due to shearing of the plug. This failure mode is commonly reported in previous studies including penetration of blunt tip penetrators [28–30]. It is also noted in Fig. 5 that the force–displacement curves of quasi-static force–displacement curves are very close, strain rate independent, while the force in the intermediate impact velocity test decreases below those of quasi-static tests after 4 mm displacement. This is somewhat related with the increased thinning rate of plug edges at higher strain rates as the main deformation mode at both velocity levels is the shear-based plug formation. As can be seen from the negative D_4 (indicating the effect of strain rate on failure strain) constant, the failure strain value of 304L stainless steel material decreases with the increase in strain rate. It is thought that the decrease in the force level in the dynamic tests is due to the decrease in the failure strain value.

The force–displacement curves and the pictures of a deformed S1 specimen against conical tip penetrator is shown in Fig. 6. Again, the force–displacement curves at quasi-static velocities are almost the same, while the force in the intermediate impact velocity test decreases below those of quasi-static tests after 2 mm displacement. The deformation pictures shown in Fig. 6 indicate that the conical tip penetrator results in a more localized hemispherical cap deformation than the blunt tip penetrator (c in Fig. 6). Further penetration after the point c in Fig. 6 results in tearing of inward folded spherical section at around 2 mm displacement. Damage progress tends to follow the trend of symmetrical tearing and compression of spherical segment simultaneously (e and f Fig. 6) indicating a rapid force increase up to failure. As can be seen from Fig. 6, the displacement value at which the first localized tearing occurs has decreased due to the decrease in the failure strain value due to the increase in the strain rate.

Force–displacement curves of S1 specimen and the pictures of a deformed sample against hemispherical tip penetrator at different strain

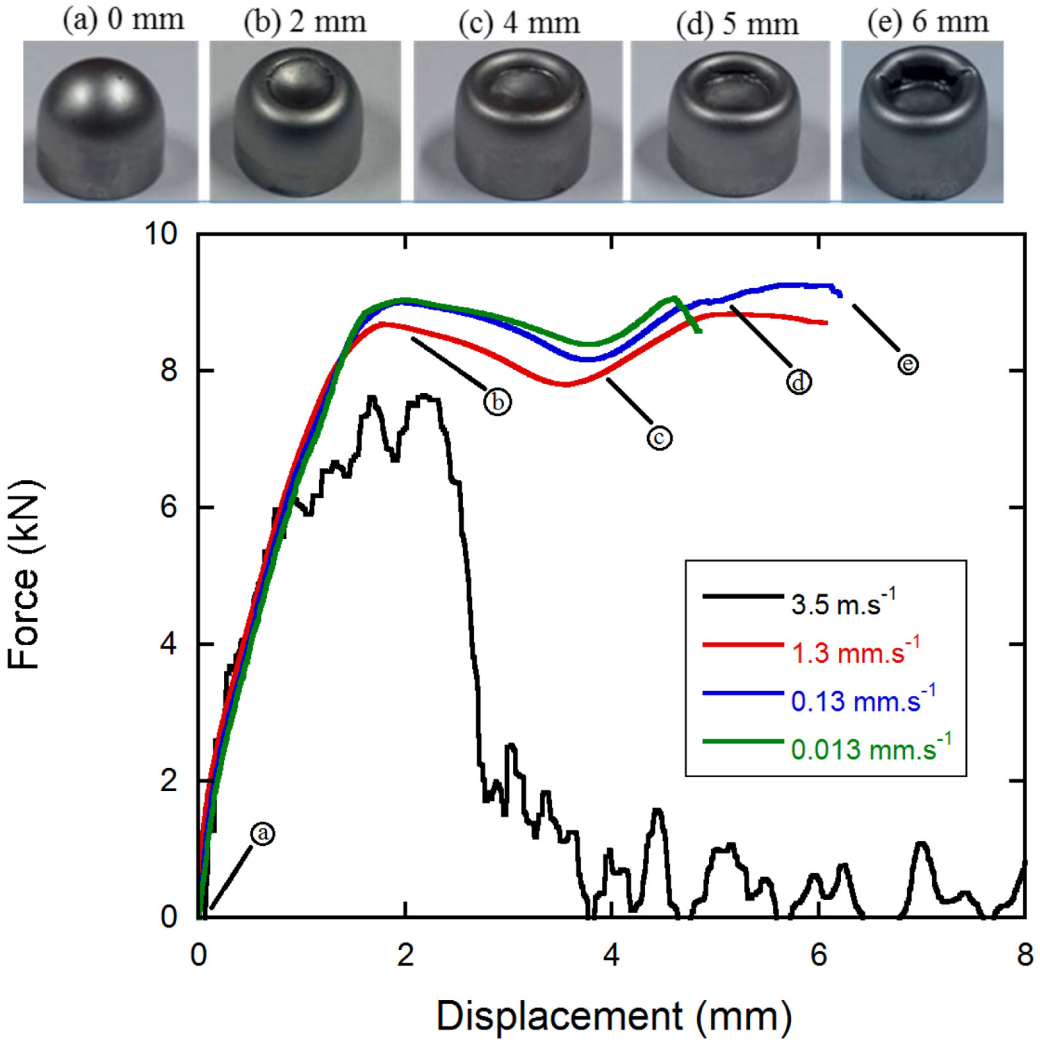

Fig. 8. Damage progress of S2 specimen against blunt tip penetrator.

rates are shown in Fig. 7. Again, there is no strain sensitivity in the force–displacement curves at the quasi-static velocity range with the use of hemispherical tip penetrator. The bi-linear portion of force–displacement curves refers to the compression-like behavior rather than penetration and the first three deformation pictures shown in Fig. 7 (corresponding to the points of a, b and c in the force–displacement curve) indicate the global plastic deformation of both hemispherical and cylindrical segments with a progressive inward dimpling on the longitudinal direction.

The force–displacement curves and the pictures of a deformed S2 specimen against blunt tip penetrator at low and intermediate impact velocities are shown in Fig. 8. A local maximum force is reached at a displacement of 2 mm (b in Fig. 8), followed by a sudden decrease of force due to initiation of progressive inward bending of spherical cap. Formation of a plug with small size radial tear is noted at increasing displacements (c and d in Fig. 8), followed by the failure of specimen (e in Fig. 8). The force values of S2 specimens against blunt tip penetrator are also noted to decrease as the penetration velocity increases from 0.01 mm s^{-1} to 3.5 m s^{-1}. Detailed comments on this subject are given in the section where the numerical model results are presented.

Force–displacement curves of S2 specimen against conical tip penetrator at low and intermediate penetrator velocities are shown in Fig. 9. It is seen in the graphs that, along with penetrator velocity dependency, S2 specimen indicates a change both in shape of force–displacement curves and damage formation throughout the displacement-controlled tests. As shown in Fig. 9, first two images (a) and (b) of damage progress indicate the indentation of penetrator tip to the hemispherical cap. Local damage due to tearing is also noted for both of the specimens and it is followed by petaling as in Fig. 9 (d1 at the cross-head speed of 0.013 mm·s^{-1}), while symmetrical tearing is observed at the cross-head speed of 0.13 mm·s^{-1} (d2 in Fig. 9). Compared to the S1 sample, with the increase in thickness in the S2 sample, strain rate sensitivity is observed even in quasi-static tests from the point of the first tearing. In the dynamic test results, the decrease in the failure strain value due to the increase in the strain rate shows itself with the formation of the first peak in the dynamic force–displacement curve at lower displacement values. Similarly, this tear rapidly expanded in the manner of petal formation, and the force value increased rapidly at low displacement levels.

Force–displacement curves of S2 specimen against hemispherical tip penetrator at low penetrator velocities are shown in Fig. 10. Results indicate that the shape of force–displacement curves and damage have similar characteristics with S1 specimen, and S2 samples also shows a compressive-like behavior with global plastic deformation (a–d in Fig. 10), followed by radial shearing of inward folded cylindrical segment (e in Fig. 10). It is also noted that force–displacement curves of S2 specimen show a velocity independent behavior when subjected to the penetration against hemispherical tip penetrator.

The experimental and numerical values of the forces and energies of the penetration tests are tabulated in Table 2. In this table, P_i is the initial peak force, P_m is the mean force, P_{max} is the maximum force, AEF is the absorbed energy up to failure and SAE is the specific absorbed

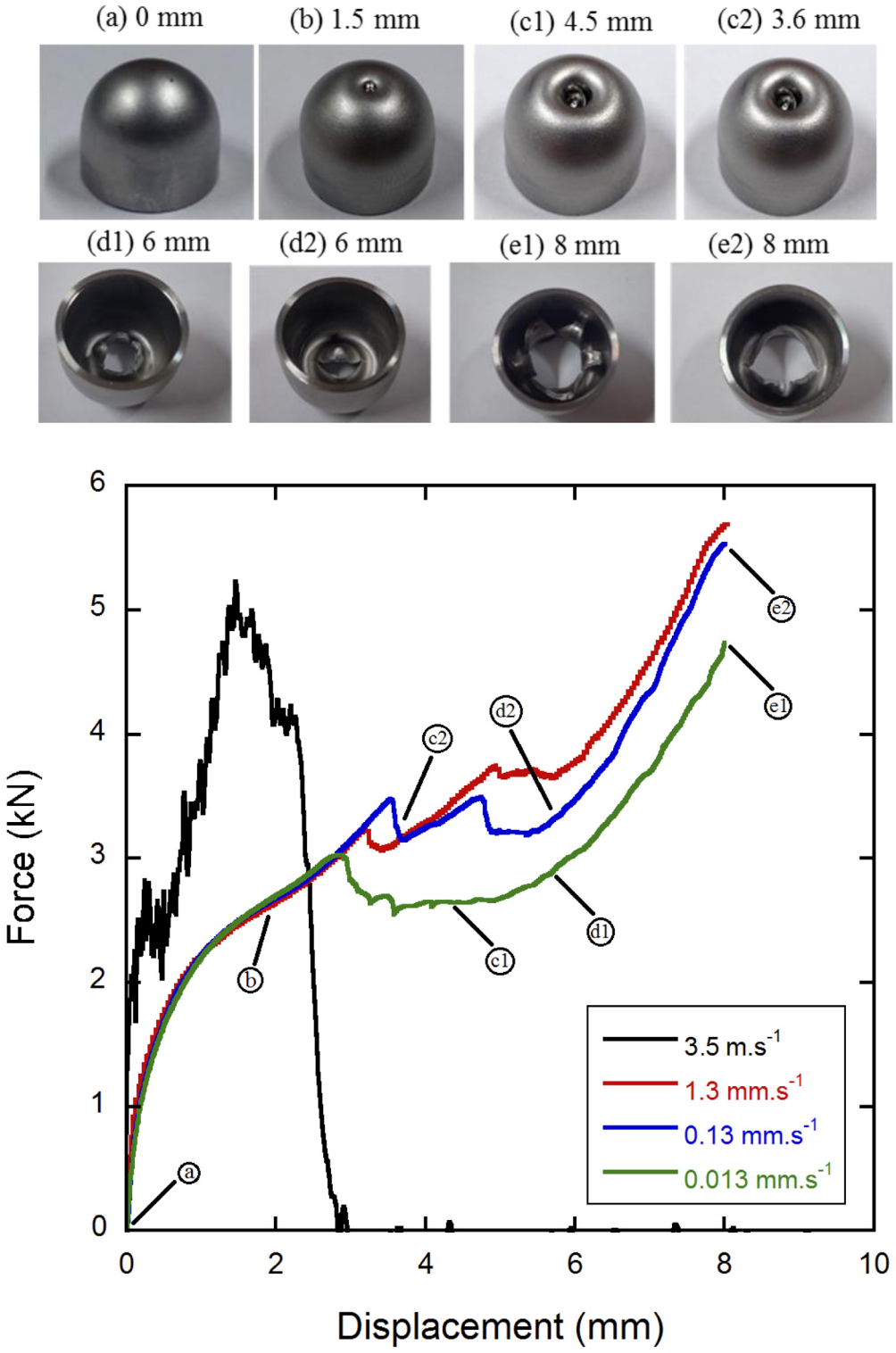

Fig. 9. Damage progress of S2 specimen against conical tip penetrator.

energy (the ratio of absorbed energy to weight of the structure). The highest AEF value of S1 core unit is observed in the tests against blunt tip penetrator with an average of 39.91 J, followed by hemispherical and conical penetrators with the averages of 30.13 J and 8.05 J, respectively. AEF parameter tends to increase with increasing the thickness of core units. However, the increase in thickness results in a reduced SAE due to weight increase of core units and tests of S2 core units against blunt tip indenter shows lower SAE values regardless of the test type. Highest AEF value of S2 core units occurs against hemispherical penetrator with an average of 93.96 kJ/kg. Tests against blunt and conical tip penetrators are followed the aforementioned results with AEF averages of 46.79 kJ/kg and 26.86 kJ/kg, respectively. AEF and SAE values tend to decrease with increasing penetrator velocity from

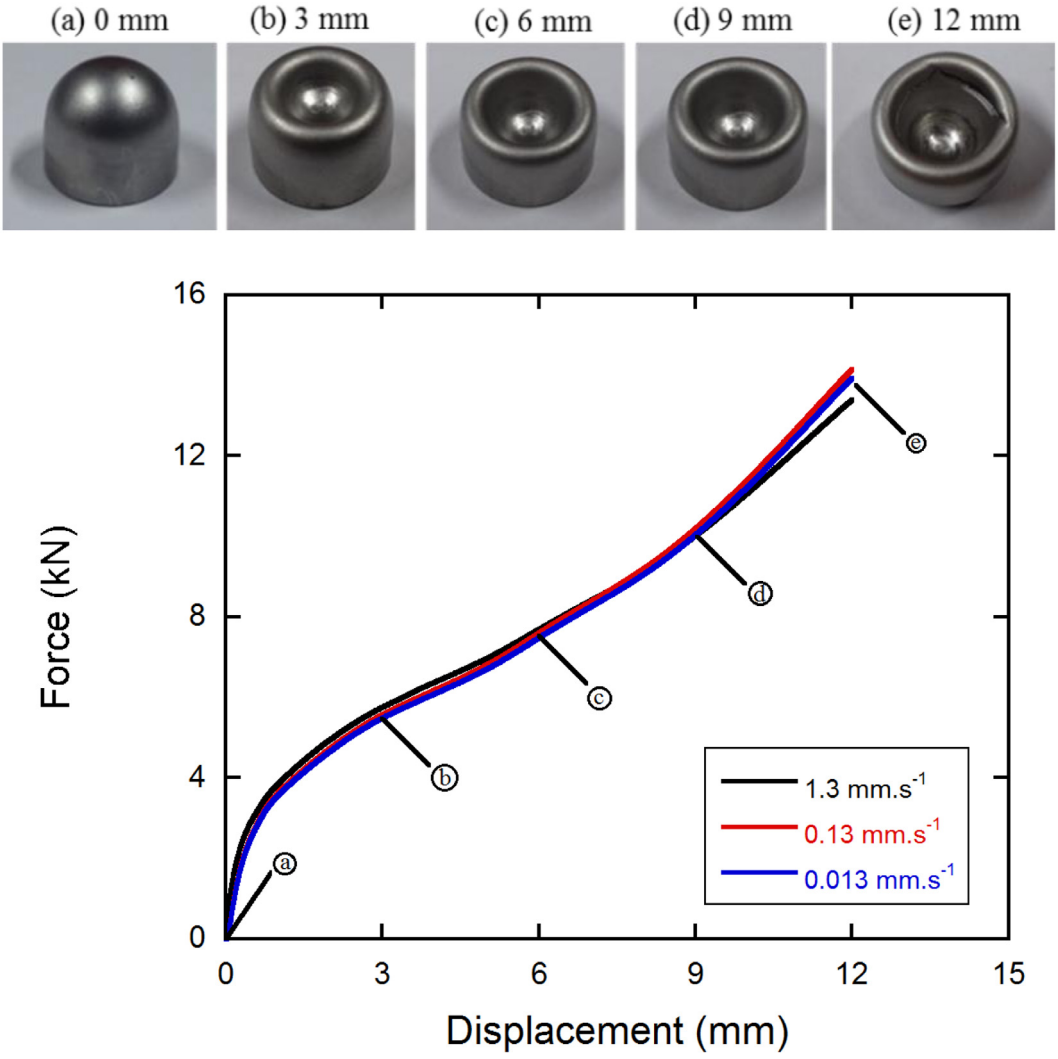

Fig. 10. Damage progress of S2 specimen against hemispherical tip penetrator.

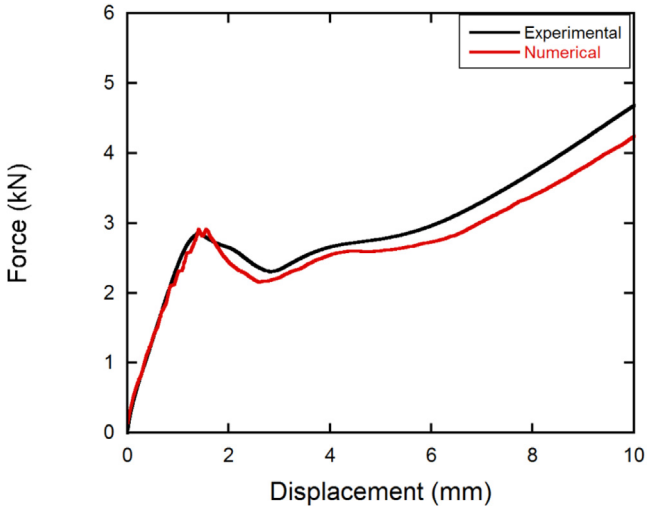

Fig. 11. Comparison of experimental and numerical behavior of S1 structure.

quasi-static to drop weight tests except the tests of S1 core units against conical tip penetrator.

4.2. Numerical results

The numerical force–displacement curve of S1 specimen against blunt tip penetrator at 1.3 mm s^{-1} penetrator velocity is shown in Fig. 11, together with that of an experimental force–displacement curve. An acceptable agreement is seen between the numerical and experimental force–displacement curves. A small difference noted in the maximum force may be correlated with the difference between the actual and numerical thicknesses of the structure [24]. Residual stresses resulting from forming operations may lead to differences in the thicknesses. The experimental and numerical deformation profiles of core structures at increasing displacements are also very similar to each other as shown in Fig. 12.

The numerical and experimental intermediate velocity force–displacement curves of S2 core structure with blunt penetrator are shown in Fig. 13. The numerical force–displacement curve shows a good correlation with the experimental one. As commented previously, S2 specimens show reduced forces and maximum force at increasing velocities against blunt penetrator. Numerical study reveals that, the thickness of deformed area tends to decrease with the displacement of penetrator. The initial thickness in model is around 0.80 mm while the

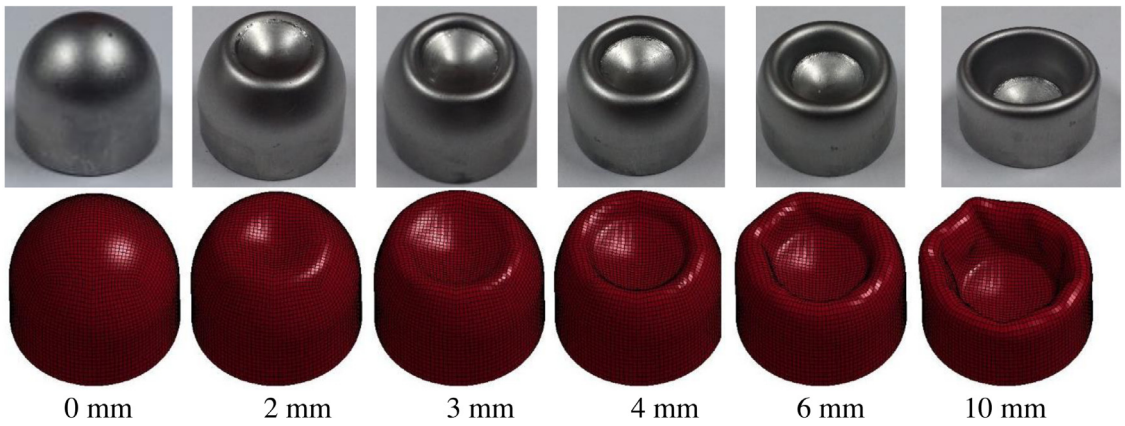

Fig. 12. Comparison of experimental and numerical deformation profiles of S1 structure.

Table 2
Experimental and numerical results.

Specimen type	Penetrator type	Test type	Result	P_i (kN)	P_m (kN)	P_{max} (kN)	AEF (J)	SAE (kJ/kg)
S1	Blunt	Quasi-static	Experimental	2.86	3.30	5.63	39.91	20.78
			Numerical	2.92	2.97	4.91	36.49	19.05
S1	Conical	Quasi-static	Experimental	0.91	1.04	1.94	8.05	4.18
			Numerical	0.94	0.98	1.75	8.74	4.55
S1	Hemispherical	Quasi-static	Experimental	0.61	2.51	4.77	30.13	15.69
			Numerical	0.66	2.21	4.18	26.55	13.83
S1	Blunt	Drop weight	Experimental	2.87	2.62	3.95	31.63	16.47
			Numerical	2.81	2.91	4.16	33.71	17.55
S1	Conical	Drop weight	Experimental	0.80	1.04	1.85	9.02	4.69
			Numerical	0.76	1.03	1.89	9.03	4.70
S2	Blunt	Quasi-static	Experimental	8.68	7.84	8.83	46.79	13.60
			Numerical	9.29	7.73	9.29	47.33	13.76
S2	Conical	Quasi-static	Experimental	3.23	3.35	5.68	26.89	7.81
			Numerical	2.18	3.32	5.81	25.64	7.45
S2	Hemispherical	Quasi-static	Experimental	4.82	7.83	13.39	93.96	27.32
			Numerical	4.32	7.61	12.62	91.38	26.56
S2	Blunt	Drop weight	Experimental	6.21	5.17	8.24	17.82	5.18
			Numerical	8.02	5.51	9.01	15.71	4.56
S2	Conical	Drop weight	Experimental	2.8	3.15	5.25	9.29	2.70
			Numerical	2.05	4.07	5.18	12.1	3.51

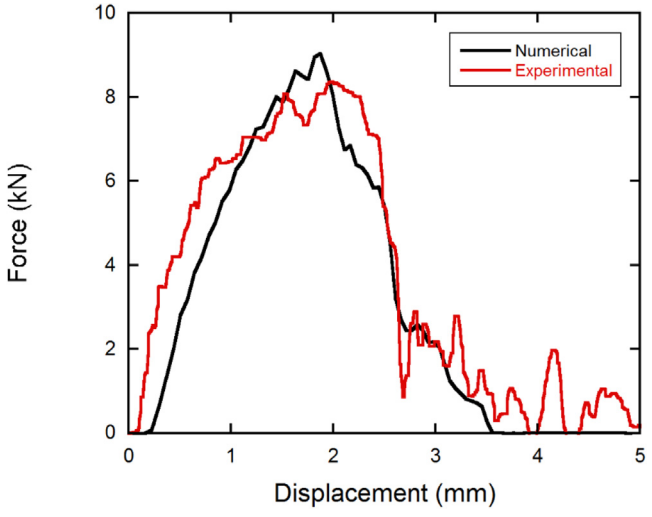

Fig. 13. Comparison of experimental and numerical behavior of S2 structure at intermediate velocity range.

thickness decreases to 0.6 mm, when the plug formation starts. The decrease in thickness is seen as tearing at points in contact with the penetrator, which results in decrease of maximum force with increasing velocity. Initial and final thickness of the torn piece are shown in Figs. 14(a) and (b), respectively.

4.3. Strain rate and micro-inertia effects

Having seen the validity of the numerical models with experimental studies, the study continued with this section, in which higher impact rates were included and different mechanisms were examined. The crushing behavior of thin-walled structures defines the classification of energy absorbing structures as Type I and Type II [31,32]. The force–displacement curves with a relatively flat-topped form is classified as Type I, whereas the force–displacement curves with a steep decline are classified as Type II. Type II structures are more sensitive to strain rate and micro-inertia than Type I. The energy absorption capability of Type II structures increase more rapidly with the strain rate sensitivity of base material [32]. As the investigated core structure includes both Type I (hemispherical segment) and Type II (cylindrical segment) portions, the effects of micro-inertia and strain rate were numerically investigated by conducting additional FEA work at increasing penetrator velocities. The effect of strain rate was investigated by the difference between the force–displacement curves under quasi-static and high

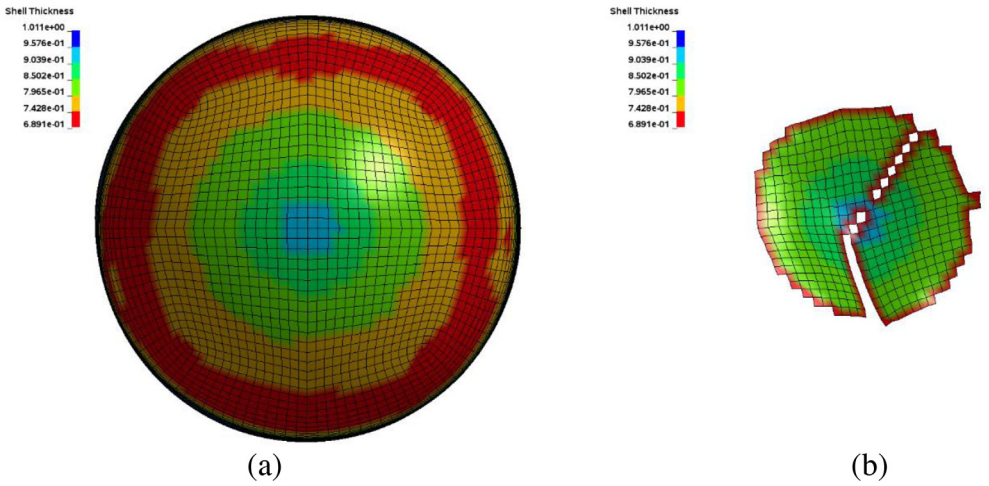

Fig. 14. Initial (a) and final (b) thicknesses of deformed area at intermediate velocity range.

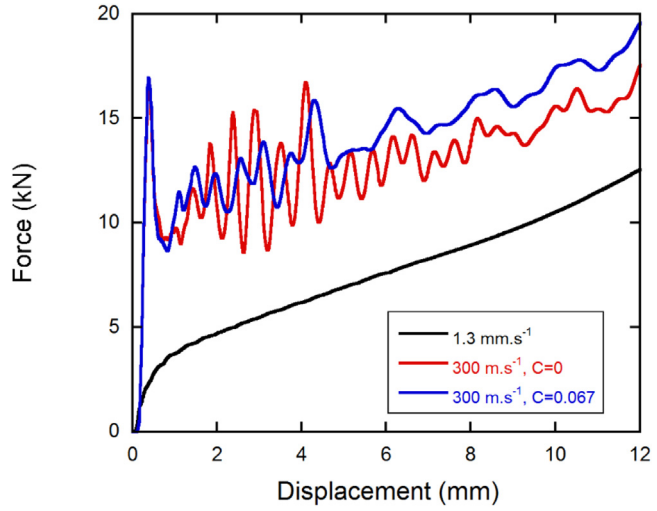

Fig. 15. Effect of strain rate and micro-inertia on S2 core structure against hemispherical tip penetrator.

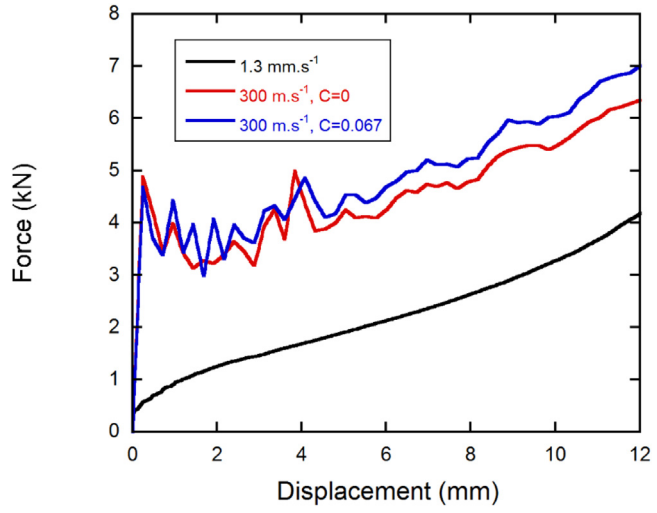

Fig. 16. Effect of strain rate and micro-inertia on S1 core structure against hemispherical tip penetrator.

velocity penetration, while the effect of micro-inertia was investigated under high velocity penetration by setting the strain rate parameter on and off for deforming structure's material model. Therefore, the influence of the loading rate on the penetration/perforation behavior is not only a material strain rate effect, but also is related to local dynamic effects induced by the rapid deformation of the thin-walled structure i.e., micro-inertia.

In order to investigate the aforementioned effects, finite element models of S2 structure against hemispherical tip penetrator were taken as a case study. The strain rate and micro-inertia effects were investigated by increasing the penetrator velocity to 300 m·s^{-1} and setting the strain rate parameter to 0.067 and 0 in the Johnson–Cook material model. Comparison of force–displacement curves for strain rate and micro-inertia effects are shown in Fig. 15. As depicted in the same graph, it has been observed that the strain rate is not very effective on the dynamic penetration behavior, especially at low deformation levels. In other words, it can be said that the increase in the dynamic curve when compared to the static curve is mainly due to micro inertia. However, with the progression of the deformation (after ~3 mm of displacement), the global deformation occurring in the sample also increases and it is observed that the strain-rate sensitivity of the material also becomes more effective after this point.

Strain rate and micro-inertia effects were also investigated for S1 core structure against hemispherical tip penetrator and results are shown in Fig. 16. Again, the penetrator velocity is selected 300 m s^{-1}. Again, in this case, a behavior similar to the S1 sample was observed. Reducing the thickness has brought the displacement value, where the strain rate sensitivity comes into play, to about 4 mm. However, with the progression of the deformation, the efficiency of the strain rate sensitivity increases again. Since the sharpness of the hemispherical tip is blunt than the conical tip, the initial stages of the penetration behavior are quite similar to the crushing behavior of this structure. Similarly, in the study in which the crushing properties of the aforementioned structure were examined [24], it was observed that the micro-inertia effect was more dominant in the increase in force at the initial stages of the deformation.

5. Conclusions

The penetration behavior of combined geometry core structures with different penetrator tip geometries was investigated experimentally and numerically at varying penetrator velocities. The strain rate sensitivity in the material model and the residual stress and strain levels in the numerical model were both included in the numerical analysis. Experiments showed that, regardless of the penetrator geometry, penetration behavior of S1 core units were not affected with

the changes in penetrator velocity, while S2 core units were found to be affected with changes in the penetrator velocity against blunt and conical tip penetrators. Increasing the thickness of core geometry resulted in an overall increase in P_i, P_m and P_{max} values. AEF values were found to increase with the increase of core unit thickness but SAE was found to decrease with the increase of thickness against blunt tip penetrator. Additional numerical studies were conducted on a single case where core units were subjected to penetration of hemispherical tip penetrator at 300 m s^{-1} to investigate the effect of strain rate and micro-inertia. Behavior of core units showed that strain rate effects were more dominant at increased penetrator velocities and micro-inertia effect was much pronounced at the displacements above 4 mm for thicker and 5 mm for thinner core units. In this study, impact location was in the center of a single core unit, for future work the effect of impact location and the multiple core unit configurations will also be investigated.

CRediT authorship contribution statement

Ali Kivanc Turan: Software, Methodology, Investigation, Data curation. **Alper Tasdemirci:** Writing – original draft, Validation, Software, Project administration, Methodology, Investigation, Conceptualization. **Ali Kara:** Validation, Software, Investigation. **Selim Sahin:** Validation, Software, Investigation. **Mustafa Guden:** Writing – original draft, Validation, Investigation.

Declaration of competing interest

The authors declare that they have no known competing financial interests or personal relationships that could have appeared to influence the work reported in this paper.

Data availability

Data will be made available on request.

Acknowledgment

The authors would like to thank the Scientific and Technical Council of Turkey (TUBITAK) for the Grant # 112M141

References

[1] T. Børvik, S. Dey, A.H. Clausen, Perforation resistance of five different high-strength steel plates subjected to small-arms projectiles, Int. J. Impact Eng. 36 (2009) 948–964.
[2] T. Børvik, M. Langseth, O.S. Hopperstad, K.A. Malo, Ballistic penetration of steel plates, Int. J. Impact Eng. 22 (1999) 855–886.
[3] T. Børvik, M. Langseth, O.S. Hopperstad, K.A. Malo, Perforation of 12 mm thick steel plates by 20 mm diameter projectiles with flat, hemispherical and conical noses: Part I: Experimental study, Int. J. Impact Eng. 27 (2002) 19–35.
[4] M.A. Abdel-Wahed, A.M. Salem, A.S. Zidan, A.M. Riad, Penetration of a small caliber projectile into single and multi-layered targets, in: F. Bremand (Ed.), ICEM 14, in: 14th International Conference on Experimental Mechanics, vol. 6, 2010.
[5] N.K. Gupta, V. Madhu, An experimental study of normal and oblique impact of hard-core projectile on single and layered plates, Int. J. Impact Eng. 19 (1997) 395–414.
[6] X.-s. Kong, W.-g. Wu, J. Li, P. Chen, F. Liu, Experimental and numerical investigation on a multi-layer protective structure under the synergistic effect of blast and fragment loadings, Int. J. Impact Eng. 65 (2014) 146–162.
[7] A. Tasdemirci, I.W. Hall, Numerical and experimental studies of damage generation in multi-layer composite materials at high strain rates, Int. J. Impact Eng. 34 (2007) 189–204.
[8] C.J. Yungwirth, H.N.G. Wadley, J.H. O'Connor, A.J. Zakraysek, V.S. Deshpande, Impact response of sandwich plates with a pyramidal lattice core, Int. J. Impact Eng. 35 (2008) 920–936.
[9] B.L. Buitrago, C. Santiuste, S. Sánchez-Sáez, E. Barbero, C. Navarro, Modelling of composite sandwich structures with honeycomb core subjected to high-velocity impact, Compos. Struct. 92 (2010) 2090–2096.
[10] W. Hou, F. Zhu, G. Lu, D.-N. Fang, Ballistic impact experiments of metallic sandwich panels with aluminium foam core, Int. J. Impact Eng. 37 (2010) 1045–1055.
[11] S. Feli, M.H. Namdari Pour, An analytical model for composite sandwich panels with honeycomb core subjected to high-velocity impact, Composites B 43 (2012) 2439–2447.
[12] C. Kılıçaslan, M. Güden, İ.K. Odacı, A. Taşdemirci, The impact responses and the finite element modeling of layered trapezoidal corrugated aluminum core and aluminum sheet interlayer sandwich structures, Mater. Des. 46 (2013) 121–133.
[13] A. Kolopp, S. Rivallant, C. Bouvet, Experimental study of sandwich structures as armour against medium-velocity impacts, Int. J. Impact Eng. 61 (2013) 24–35.
[14] H.N.G. Wadley, K.P. Dharmasena, M.R. O'Masta, J.J. Wetzel, Impact response of aluminum corrugated core sandwich panels, Int. J. Impact Eng. 62 (2013) 114–128.
[15] L. Jing, Z. Wang, L. Zhao, Response of metallic cylindrical sandwich shells subjected to projectile impact—Experimental investigations, Compos. Struct. 107 (2014) 36–47.
[16] G. Jiga, Ş. Stamin, G. Dinu, T. Dobrescu, D. Popovici, Comparative studies on the impact behavior of two sandwich structures, Procedia Eng. 100 (2015) 418–427.
[17] M.-m. Xu, G.-y. Huang, S.-s. Feng, X.-y. Qin, G.J. McShane, W.J. Stronge, Perforation resistance of aluminum/polyethylene sandwich structure, Mater. Des. 100 (2016) 92–101.
[18] A. Alavi Nia, S. Mokari, M. Zakizadeh, M. Kazemi, Experimental and numerical investigations of the effect of cellular wired core on the ballistic resistance of sandwich structures, Aerosp. Sci. Technol. 70 (2017) 445–452.
[19] L. Zhu, K. Guo, Y. Li, T.X. Yu, Q. Zhou, Experimental study on the dynamic behaviour of aluminium foam sandwich plates under single and repeated impacts at low temperature, Int. J. Impact Eng. 114 (2018) 123–132.
[20] N. Jover, B. Shafiq, U. Vaidya, Ballistic impact analysis of balsa core sandwich composites, Composites B 67 (2014) 160–169.
[21] H. Zhao, I. Elnasri, Y. Girard, Perforation of aluminium foam core sandwich panels under impact loading—An experimental study, Int. J. Impact Eng. 34 (2007) 1246–1257.
[22] A. Tasdemirci, G. Tunusoglu, M. Güden, The effect of the interlayer on the ballistic performance of ceramic/composite armors: Experimental and numerical study, Int. J. Impact Eng. 44 (2012) 1–9.
[23] A. Tasdemirci, A. Kara, K. Turan, S. Sahin, M. Guden, Effect of heat treatment on the blast loading response of combined geometry shell core sandwich structures, Thin-Walled Struct. 100 (2016) 180–191.
[24] A. Tasdemirci, S. Sahin, A. Kara, K. Turan, Crushing and energy absorption characteristics of combined geometry shells at quasi-static and dynamic strain rates: Experimental and numerical study, Thin-Walled Struct. 86 (2015) 83–93.
[25] A. Tasdemirci, A. Kara, K. Turan, S. Sahin, Dynamic crushing and energy absorption of sandwich structures with combined geometry shell cores, Thin-Walled Struct. 91 (2015) 116–128.
[26] 7.62 × 51 mm NATO AP technical details, 2022.
[27] L.S.T. Corporation, LS-DYNA Keyword User's Manual.
[28] T. Børvik, J.R. Leinum, J.K. Solberg, O.S. Hopperstad, M. Langseth, Observations on shear plug formation in weldox 460 E steel plates impacted by blunt-nosed projectiles, Int. J. Impact Eng. 25 (2001) 553–572.
[29] V.F. Nesterenko, W. Goldsmith, S.S. Indrakanti, Y. Gu, Response of hot isostatically pressed Ti–6Al–4V targets to normal impact by conical and blunt projectiles, Int. J. Impact Eng. 28 (2003) 137–160.
[30] X.W. Chen, Y.B. Yang, Z.H. Lu, Y.Z. Chen, Perforation of metallic plates struck by a blunt projectile with a soft nose, Int. J. Impact Eng. 35 (2008) 549–558.
[31] C.R. Calladine, R.W. English, Strain-rate and inertia effects in the collapse of two types of energy-absorbing structure, Int. J. Mech. Sci. 26 (1984) 689–701.
[32] L.L. Tam, C.R. Calladine, Inertia and strain-rate effects in a simple plate-structure under impact loading, Int. J. Impact Eng. 11 (1991) 349–377.